The Role of the Third Dredge-up and Mass Loss in Shaping the Initial–Final Mass Relation of White Dwarfs

Francesco Addari, Paola Marigo, Alessandro Bressan, Guglielmo Costa, Kendall Shepherd, Guglielmo Volpato

The Astrophysical Journal, 964:51 (13pp), 2024 March 20 https://doi.org/10.3847/1538-4357/ad2067

The Role of the Third Dredge-up and Mass Loss in Shaping the Initial–Final Mass Relation of White Dwarfs

Francesco Addari[1,2], Paola Marigo[3], Alessandro Bressan[1], Guglielmo Costa[4], Kendall Shepherd[1,2], and Guglielmo Volpato[2,3]
[1] Scuola Internazionale Superiore di Studi Avanzati, Via Bonomea, 265, I-34136, Trieste, Italy
[2] Osservatorio Astronomico di Padova–INAF, Vicolo dell'Osservatorio 5, I-35122 Padova, Italy
[3] Dipartimento di Fisica e Astronomia Galileo Galilei, Università degli studi di Padova, Vicolo dell'Osservatorio 3, I-35122 Padova, Italy
[4] Université Claude Bernard Lyon 1, Ens de Lyon, CNRS, Centre de Recherche Astrophysique de Lyon UMR5574, F-69230 Saint-Genis-Laval, France
Received 2023 December 11; revised 2024 January 16; accepted 2024 January 17; published 2024 March 14

Abstract

The initial–final mass relation (IFMR) plays a crucial role in understanding stellar structure and evolution by linking a star's initial mass to the mass of the resulting white dwarf. This study explores the IFMR in the initial mass range $0.8 \leqslant M_{\rm ini}/M_{\odot} \leqslant 4$ using full PARSEC evolutionary calculations supplemented with COLIBRI computations to complete the ejection of the envelope and obtain the final core mass. Recent works have shown that the supposed monotonicity of the IFMR is interrupted by a kink in the initial mass range $M_{\rm ini} \approx 1.65$–$2.10\,M_{\odot}$, due to the interaction between recurrent dredge-up episodes and stellar winds in carbon stars evolving on the thermally pulsing asymptotic giant branch phase. To reproduce the IFMR nonmonotonic behavior we investigate the role of convective overshooting efficiency applied to the base of the convective envelope ($f_{\rm env}$) and to the borders of the pulse-driven convective zone ($f_{\rm pdcz}$), as well as its interplay with mass loss. We compare our models to observational data and find that $f_{\rm env}$ must vary with initial mass in order to accurately reproduce the IFMR's observed kink and slopes. We find some degeneracy between the overshooting parameters when only the IFMR information is used. Nonetheless, this analysis provides valuable insights into the internal mixing processes during the TP-AGB phase.

Unified Astronomy Thesaurus concepts: Asymptotic giant branch stars (2100); Carbon stars (199); White dwarf stars (1799); Stellar winds (1636); Stellar convective zones (301)

1. Introduction

The thermally pulsing asymptotic giant branch (TP-AGB) phase is the final evolutionary stage of low- and intermediate-mass stars ($0.8 \lesssim M_{\rm ini}/M_{\odot} \lesssim 7$–$8$), which ends when the envelope is ejected by stellar winds in the interstellar medium and the bare central core cools as a carbon–oxygen (CO) white dwarf (Herwig 2005; Karakas & Lattanzio 2014).

The evolution of the TP-AGB phase is heavily influenced by processes that are difficult to model from first principles, such as turbulent convection, stellar winds, long-period variability, and various dredge-up episodes (collectively designated as the third dredge-up, or TDU). Furthermore, these processes interact with one another and do not occur smoothly during the TP-AGB evolution, but they may vary greatly in characteristics and efficiency over a thermal pulse cycle.

We recall that the TDU is responsible for the formation of carbon stars, characterized by a photospheric C/O ratio higher than 1. In fact, at the stage of the maximum luminosity produced by the thermal instabilities of the He-burning shell, the bottom of the convective envelope may stretch inside the region involved in the thermal pulse nucleosynthesis, bringing newly synthesized carbon produced by the triple-alpha reaction to the surface (Herwig 2005). Unfortunately, the TDU is highly dependent on the physics prescription and numerical treatment (Frost & Lattanzio 1996; Mowlavi 1999) of the stellar evolution code, resulting in a wide heterogeneity of TP-AGB models and results (Herwig 2000; Stancliffe et al. 2005; Weiss & Ferguson 2009; Cristallo et al. 2011; Marigo et al. 2013; Karakas 2014; Ventura et al. 2018).

One method for constraining the efficiency of the TDU is to reproduce the carbon star luminosity functions in various galaxies with different age–metallicity relations and known star formation histories (Groenewegen & de Jong 1993; Marigo et al. 1999; Marigo & Girardi 2007; Pastorelli et al. 2019, 2020).

The semiempirical initial–final mass relation (IFMR) of CO white dwarfs provides another approach to calibrating the TDU in Milky Way carbon stars, as demonstrated in a few studies (Kalirai et al. 2014; Marigo et al. 2020; Marigo 2022a).

Following the exploration in these works, this research focuses on the semiempirical IFMR, with the goals of reproducing semiempirical behavior using recent data and retrieving information on the TDU using full self-consistent TP-AGB stellar models. To recover the semiempirical IFMR, we will specifically investigate the role of mass loss and convective overshooting applied to the base of the convective envelope and the borders of the pulse-driven convective zone (PDCZ).

The IFMR is an important tool for understanding stellar evolution because it provides insight into the processes that occur during a star's lifetime, in particular setting constraints on the amount of mass lost by stellar winds (Marigo 2013, 2022a, 2022b; Kalirai et al. 2014).

In general, the IFMR predicts that more massive stars will produce more massive remnants. Over the years improvements on the semiempirical IFMR have been achieved thanks to new observations and refined treatments in stellar evolution codes

(Weidemann 2000; Williams et al. 2004, 2009; Kalirai et al. 2008, 2009, 2014; Salaris et al. 2009; Cummings et al. 2018, 2019 and references therein).

Recently, with the addition of new white dwarf data belonging to open clusters with ages of 1.5–2.5 Gyr, Marigo et al. (2020) found a kink in the IFMR at $M_{\rm ini} \simeq 1.65$–$2.10\,M_{\odot}$ that suddenly interrupts the commonly assumed monotonic behavior. Surprisingly, the white dwarfs at the peak, which are all members of the open cluster NGC 7789, reach masses of $\simeq$0.70–0.74 $M_{\odot}$, which have previously been associated with stars with $M_{\rm ini} \simeq 3\,M_{\odot}$.

The IFMR kink is interpreted as a signature of the lowest-mass stars in the Milky Way that evolved into carbon stars during the TP-AGB phase. According to Marigo et al. (2020), these carbon stars are expected to have undergone shallow TDU events, resulting in low photospheric C/O and modest carbon excess with respect to oxygen. Under these conditions, carbonaceous dust grains cannot condense in sufficient quantities to cause a strong wind, so the TP-AGB lifetime is prolonged and the core mass can grow more than usually predicted. Theoretically, the key to this behavior is the use of mass-loss prescriptions for carbon stars that are dependent on carbon excess, which are based on state-of-the-art dynamical models (Mattsson et al. 2010; Eriksson et al. 2014; Bladh et al. 2019).

An independent study of AGB stars in Galactic open clusters using Gaia EDR3 recently confirmed these findings (Marigo et al. 2022a). In the initial mass range of the kink, the study found carbon stars with dust-free spectra and irregular small-amplitude pulsations (implying very low mass loss as estimated from spectral energy distribution fitting) with current core masses of $\simeq$0.67–0.7 $M_{\odot}$, consistent with white dwarf masses (see Figure 8 of that paper).

The paper is structured as follows. Section 2 presents and discusses the input physics and technical details of our PARSEC models. In Section 3, we recall the evolutionary properties of low- and intermediate-mass stars with references to our tracks. Section 4 describes how to estimate the final mass of the white dwarf and the shape of the IFMR. Our concluding remarks end the paper in Section 5.

2. Input Physics

The code and main input physics used in PARSEC V2.0 are described thoroughly in Bressan et al. (2012), Tang et al. (2014), Chen et al. (2014), Fu et al. (2018), Costa et al. (2019a, 2019b), and Nguyen et al. (2022). Here we summarize the relevant points for the low- and intermediate-mass stars treated in this work.

Our sets of TP-AGB tracks have solar-like metallicity $Z = 0.014$, with a solar-scaled chemical composition from Caffau et al. (2011). The helium content is given by $Y = Z \cdot \Delta Y/\Delta Z + Y_{\rm p} = 0.273$ with $Y_{\rm p} = 0.2485$ (Komatsu et al. 2011) and $\Delta Y/\Delta Z = 1.78$ (Bressan et al. 2012). Equation-of-state tables are calculated using the FREEEOS code developed by A. W. Irwin.[5] Nuclear reaction rates include a total of 72 reactions and track 32 isotopes: ^{1}H, D, ^{3}He, ^{4}He, ^{7}Li, ^{7}Be, ^{12}C, ^{13}C, ^{14}N, ^{15}N, ^{16}O, ^{17}O, ^{18}O, ^{19}F, ^{20}Ne, ^{21}Ne, ^{22}Ne, ^{23}Na, ^{24}Mg, ^{25}Mg, ^{26}Mg, ^{27}Al, ^{28}Al, ^{29}Si, ^{30}S, ^{31}Ar, ^{40}Ca, ^{44}Ti, ^{48}Cr, ^{52}Fe, ^{56}Ni, and ^{60}Zn. The primary energy-generating nuclear reactions are all included; a list with references can be found in Table 1 of Fu et al. (2018) and Costa et al. (2021). We now detail the physics inputs and go over all of the updates for dealing with the TP-AGB phase.

Opacity tables in the low-temperature regime ($\log(T/{\rm K}) < 4.2$) are calculated with ÆSOPUS (Marigo & Aringer 2009; Marigo et al. 2022b) and are updated to track the variation of carbon, nitrogen, and oxygen abundances due to consecutive dredge-up events and hot-bottom burning. In the high-temperature regime, $4.2 \leqslant \log(T/{\rm K}) \leqslant 8.7$, we use the opacity tables provided by the Opacity Project at Livermore (OPAL; Iglesias & Rogers 1996). Conductive opacities are incorporated following Itoh et al. (2008).

The nuclear reaction network and mixing are solved together with diffusive equations (Costa et al. 2019b). Regions unstable to convection are defined by the Schwarzschild criterion. The diffusion coefficient within these zones is derived from the mixing length theory framework (Böhm-Vitense 1958) and we adopt a mixing length parameter $\alpha = 1.74$ according to the calibration of the standard solar model (Bressan et al. 2012). The mixing length α is fixed across the whole evolution. At each border of all unstable zones we include convective overshooting. These regions are considered radiative. Moreover, core overshooting is treated as a ballistic process (Bressan et al. 1981), while the diffusion coefficient for the convective envelope and PDCZ overshooting is calculated with the scheme proposed by Herwig (2000):

$$D(r) = D_0 \exp\left(-2\frac{|r - r_0|}{f_{\rm ov} H_{\rm p}}\right), \quad r_0 = r_{\rm cnv} \pm f_{0,\rm ov} H_{\rm p}, \quad (1)$$

where $r_{\rm cnv}$ is the radial coordinate of the convective border according to the Schwarzschild criterion and $f_{0,\rm ov}H_{\rm p}$ is the distance inside the convective region at which overshooting begins to be applied and where the diffusion coefficient is equal to D_0. The minimum value of the diffusion coefficient is set to $D_{\rm min} = 10^3$ cm^2 s^{-1}, below which no mixing is allowed. For simplicity we assume $f_{\rm ov} = 2f_{0,\rm ov}$ (Choi et al. 2016). We define $f_{\rm env}$ and $f_{\rm pdcz}$, respectively, as the overshooting parameters at the bottom of the convective envelope and in the PDCZ. In the latter, convective overshooting is applied on both borders of the instability region. Previous studies have shown indications of overshooting in the PDCZ (Herwig 2000; Wagstaff et al. 2020) but there is no general agreement yet. A first-principles analysis indicates that the inertia of the convective eddies in the PDCZ is not enough to make them overcome the Schwarzschild border (Lattanzio et al. 2017). This may imply that there must be another mechanism able to mix over the canonical border of the PDCZ. Exponential overshooting is a simple and effective prescription that can overcome the canonical convective border while a more physically sound scheme is lacking.

As described by Bressan et al. (2012) and Nguyen et al. (2022), we apply core and envelope overshooting depending on the initial mass of the track. We define $M_{\rm O1}$ as the minimum initial mass that has a convective core during the main sequence. For $M_{\rm ini} < M_{\rm O1}$ we do not apply core overshooting, and $f_{\rm env} = f_{\rm env,min} = 0.033$; for $M_{\rm ini} > M_{\rm O2} = M_{\rm O1} + 0.3\,M_{\odot}$ we apply maximum core and envelope overshooting, as $\lambda_{\rm ov} = \lambda_{\rm ov,max} = 0.5$ and $f_{\rm env} = f_{\rm env,max} = 0.047$; and for $M_{\rm O1} \leqslant M_{\rm ini} \leqslant M_{\rm O2}$ both parameters ($\lambda_{\rm ov}$ and $f_{\rm env}$) scale linearly with the initial mass. We will refer to this set of models as $f_{\rm env} = 0.047^{*}$ or the "fiducial" value; $f_{\rm env,min}$ and $f_{\rm env,max}$ are

[5] http://freeeos.sourceforge.net/

the corresponding values of $\Lambda_{ov,min} = 0.5$ and $\Lambda_{ov,max} = 0.7$ calibrated on the red giant branch (RGB) bump and blue loop width for the previous envelope overshooting prescription (Alongi et al. 1991; Christensen-Dalsgaard et al. 2011; Bressan et al. 2015; Fu et al. 2018). The conversion from the previous to the exponential overshooting prescriptions is performed by matching the position and width of the RGB bump in the H-R diagram for low-mass and intermediate-mass stars. During the central He-burning phase the efficiency of core overshooting is set to $\lambda_{ov,max}$ for every initial mass, which gives consistent horizontal branch and AGB lifetimes with the R_2 ratio observed in globular clusters (Bressan et al. 1986; Constantino et al. 2016). We do not suppress the occurrence of breathing pulses (Sweigart & Demarque 1973; Castellani et al. 1985), but their efficiency decreases with the inclusion of nonlocal core overshooting (Bressan et al. 1986). We do not include the effects of rotation or magnetic fields, and the only extra mixing comes from overshooting.

Mass loss is treated as follows: We assume no stellar wind up to the end of the main sequence. Once the star leaves the main sequence and proceeds through the RGB we use the Reimers law with $\eta_R = 0.2$ (Reimers 1975). After the core He burning is complete and the early AGB begins, the stellar wind is described as a two-stage process. The entire formulation of mass loss on the AGB is taken from Marigo et al. (2020). For luminosities below the tip of the RGB, we assume the Alfvén wave–driven wind by Cranmer & Saar (2011). Above this threshold, while the photospheric C/O remains below unity, the mass loss is caused by pulsations and radiation pressure on silicate dust grains (Bloecker 1995) with $\eta_B = 0.01$. As the star surface becomes carbon-rich, with a low carbon excess with respect to oxygen, it enters a phase with little or no amounts of dust, and the stellar wind is described by pulsating models of almost dust-free atmospheres (Winters et al. 2000). Finally, when the carbon excess is large enough ($8.2 \lesssim (\mathrm{C–O})_{min} \lesssim 9.2$ depending on the current mass, luminosity, and effective temperature) to form significant amounts of carbonaceous dust we use the state-of-the-art dynamical atmosphere models by Mattsson et al. (2010), Eriksson et al. (2014), and Bladh et al. (2019).

Lastly, we develop, test, and use a shell-shifting-like treatment for accelerating the calculation during quiescent interpulses (details in the Appendix).

We calculate a total of 439 tracks distributed over 24 sets. The pre-TP-AGB evolution of each track in every set is calculated with the fiducial envelope overshooting $f_{env} = 0.047^*$, as explained above. Details are discussed in the following section. Then, each set is identified by a couple of values (f_{env}, f_{pdcz}) that refer only to the TP-AGB phase. Our sets span the values $0.047^* \leqslant f_{env} \leqslant 0.160$ and $0 \leqslant f_{pdcz} \leqslant 0.064$, as summarized in Table 1.

The tracks span the range of $0.8 \leqslant M_{ini}/M_\odot \leqslant 4$ (only a few sets extend to $M_{ini} \sim 5\,M_\odot$) and the mass step is $0.05 \leqslant \Delta M_{ini}/M_\odot \leqslant 0.3$ depending on the initial mass. Tracks close to and within the IFMR kink have a finer grid than stars outside.

The evolution is calculated from the pre-main sequence (PMS) to the furthest point in the TP-AGB (see Section 4). As in Bressan et al. (2012) the code interrupts when a star approaches the He flash and then it is restarted from a proper zero-age He-burning (ZAHB) model, with mass corresponding to the total mass left at the RGB tip. The transition is so rapid that we can assume the star does not lose mass. We calculate proper ZAHB models for our fiducial set $f_{env} = 0.047^*$. Overshooting in the PDCZ clearly does not matter at this stage. We determine that stars do experience a He flash for $M_{ini} \leqslant 1.85\,M_\odot$ with an accuracy of $0.05\,M_\odot$. We also estimate our $M_{O1} = 1.22\,M_\odot$, which corresponds to the H-burning core being convective and from which we start to apply core overshooting and the minimal value for f_{env} in our fiducial set.

Table 1
Sampled Values of (f_{env}, f_{pdcz})

f_{pdcz}	f_{env}						
	0.047*	0.056	0.064	0.096	0.128	0.144	0.160
0.000	✓	×	✓	×	✓	×	×
0.001	✓	✓	✓	✓	✓	✓	✓
0.002	✓	×	✓	×	✓	×	×
0.004	✓	×	✓	×	✓	×	×
0.008	✓	×	✓	×	✓	×	×
0.016	✓	×	✓	×	✓	×	×
0.032	✓	×	×	×	×	×	×
0.064	✓	×	×	×	×	×	×

Note. Check marks correspond to the calculated sets of tracks, and crosses to combinations of overshooting parameters that are not explored.

3. Evolutionary Properties

In this section, we highlight the evolutionary features of our models, with a specific focus on the core mass evolution. The definition of the core mass varies depending on the evolutionary stage. The evolution before the TP-AGB phase of PARSEC tracks has been thoroughly described recently by Nguyen et al. (2022). Prior to the TP-AGB phase, M_{core} is equal to the mass of the hydrogen-exhausted core. In order to include the possibility that white dwarfs may retain a thin hydrogen atmosphere on top of the He intershell and CO core (Saumon et al. 2022), we take

$$M_{core} = m(X = 0.5X_{surf}) \quad (2)$$

as the definition of the core mass in TP-AGB, where m is a generic mass coordinate, and X and X_{surf} are the hydrogen abundance at any mesh point and on the surface, respectively. We also mark the beginning of TP-AGB where the thickness of the He intershell falls below $0.1\,M_\odot$ (Dotter 2016).

3.1. Pre-TP-AGB Evolution

Figure 1 shows the evolution in the H-R diagram of a subsample of the spanned mass range until the beginning of the TP-AGB phase. With our assumptions of f_{env}, this part is common for all sets of tracks.

Before TP-AGB, the core is built up by the ashes of (core and shell) hydrogen and helium burning. The growth can be limited by the first and second dredge-up events (respectively, FDU and SDU). These are directly related to the efficiency of envelope overshooting.

Our study focuses on the core mass evolution and the final mass of the white dwarf left at the end. Our choice of setting the same f_{env} for all initial masses before TP-AGB fixes the penetration of the envelope during the FDU and SDU. Observations of the RGB bump constrain f_{env} during the FDU (Alongi et al. 1991; Fu et al. 2018); later during core He burning, f_{env} affects the extensions and positions of blue loops (Tang et al. 2014). However, there are no direct constraints for

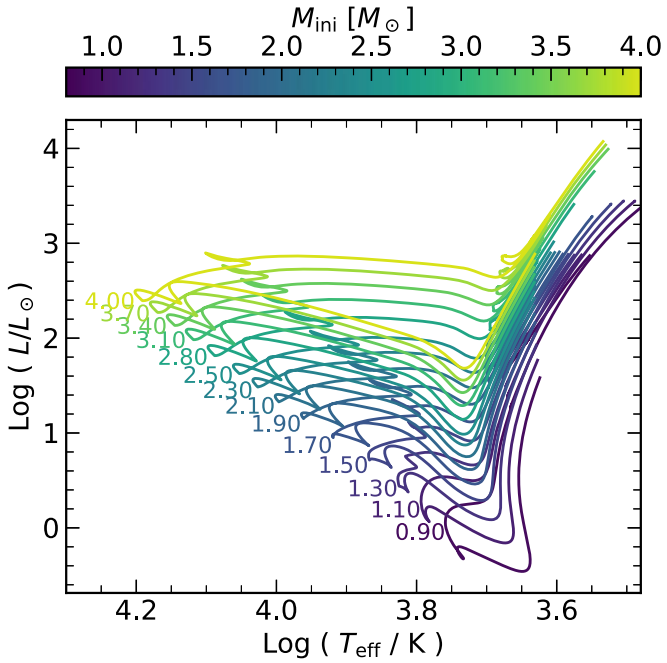

Figure 1. H-R diagram for the fiducial value of envelope overshooting and no PDCZ overshooting, from the PMS up to the onset of the TP-AGB phase. A subset is shown for clarity.

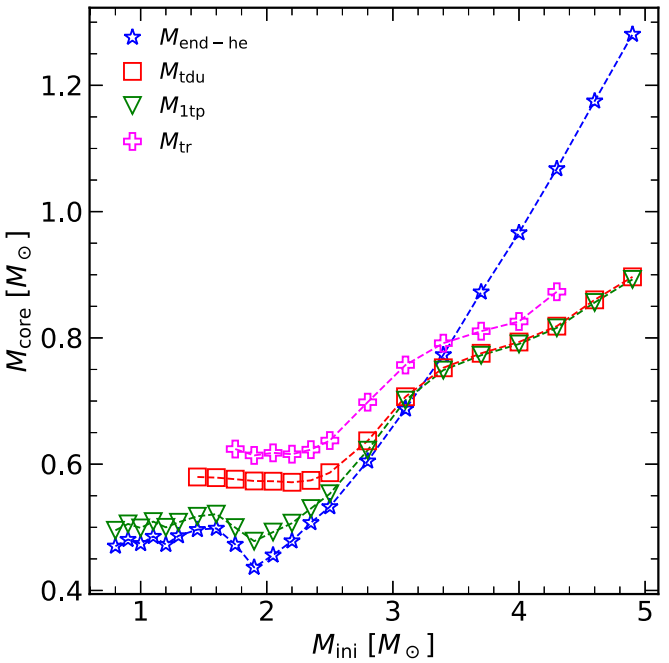

Figure 2. Core mass at different stages of the evolution for fiducial envelope overshooting and $f_{\rm pdcz} = 0.001$. $M_{\rm end-he}$ (blue stars) refers to the end of central He burning, $M_{\rm 1tp}$ (green triangles) to the first thermal pulse, $M_{\rm tdu}$ (red squares) to the first occurrence of the TDU, and $M_{\rm tr}$ (pink crosses) to the core mass at which the star moves from M-type to C-type.

the overshooting efficiency during the SDU. Therefore we want to make sure the mass of the core and the surface C/O ratio are minimally impacted by the SDU experienced by tracks with different values of $f_{\rm env}$. The SDU eventually affects stars with $M_{\rm ini} \gtrsim 3.5\,M_\odot$ (Karakas & Lattanzio 2014), and thus we calculate a few intermediate-mass star tracks by setting the $f_{\rm env}$ value from the PMS, different from the fiducial $f_{\rm env} = 0.047^*$. In Figure 2 various mass thresholds are shown with definitions in the figure caption. $M_{\rm end-he} > M_{\rm 1tp}$ reveals which tracks experience the SDU, in agreement with Karakas & Lattanzio (2014). Table 2 shows the main properties at the onset of the TP-AGB phase of two models with $M_{\rm ini} = 3.7\,M_\odot$ and $M_{\rm ini} = 4\,M_\odot$, computed with different $f_{\rm env}$ from the PMS. In particular, the core mass after the SDU and the carbon-to-oxygen ratio are the two main properties that will shape the following evolution of the track. These quantities differ by less than 2% in models with different $f_{\rm env}$ (from the PMS), and there is no clear trend with increasing overshooting penetration. Thus, we conclude that these differences may be led by purely numerical features that are intrinsic in the mixing treatment.

Our test confirms that the SDU is not appreciably affected by the choice of envelope overshooting, at least up to $M_{\rm ini} \simeq 4\,M_\odot$. Then, we modify the value of $f_{\rm env}$ only during the TP-AGB phase, ensuring consistency with previous calibrations. A PDCZ is only present during a thermal pulse, and thus the previous evolution is insensitive to $f_{\rm pdcz}$.

3.2. TP-AGB Evolution

During the TP-AGB phase, the star undergoes recurring thermal pulses driven by the thermal instability of the geometrically thin helium shell. Following each pulse, the star may experience the TDU (Herwig 2005; Karakas & Lattanzio 2014). This event reduces the core mass and transports helium-burning ashes to the surface. The efficiency of the TDU

Table 2
Track Properties at Onset of TP-AGB Phase, after SDU

$M_{\rm ini} = 3.70\,M_\odot$			
$f_{\rm env}$	0.047	0.096	0.144
$M_{\rm core}$	0.791 $M_\odot$	0.778 $M_\odot$	0.782 $M_\odot$
$X_{\rm surf}$	6.538E-01	6.522E-01	6.530E-01
$Y_{\rm surf}$	3.321E-01	3.337E-01	3.330E-01
$X_{\rm C12,surf}$	1.456E-03	1.447E-03	1.445E-03
$X_{\rm O16,surf}$	5.137E-03	5.106E-03	5.098E-03
$C/O_{\rm surf}$	3.964E-01	3.965E-01	3.964E-01
$M_{\rm ini} = 4.00\,M_\odot$			
$f_{\rm env}$	0.047	0.096	0.144
$M_{\rm core}$	0.810 $M_\odot$	0.802 $M_\odot$	0.810 $M_\odot$
$X_{\rm surf}$	6.398E-01	6.389E-01	6.388E-01
$Y_{\rm surf}$	3.462E-01	3.471E-01	3.471E-01
$X_{\rm C12,surf}$	1.423E-03	1.417E-03	1.413E-03
$X_{\rm O16,surf}$	5.011E-03	4.985E-03	4.974E-03
$C/O_{\rm surf}$	3.975E-01	3.979E-01	3.977E-01

is quantified by the parameter λ, defined as

$$\lambda = \frac{\Delta M_{\rm dup}}{\Delta M_{\rm core}} \tag{3}$$

where $\Delta M_{\rm dup}$ represents the decrease of the core mass caused by the penetration of the envelope after the ith thermal pulse. $\Delta M_{\rm core}$ is equal to the growth of the core mass between the $(i-1)$th and ith pulses. It is important to acknowledge that λ is highly sensitive to both the numerical details and the physical inputs of the model (Frost & Lattanzio 1996; Mowlavi 1999). To ensure accurate predictions, maintaining consistent numerical prescriptions is crucial when calibrating the physical

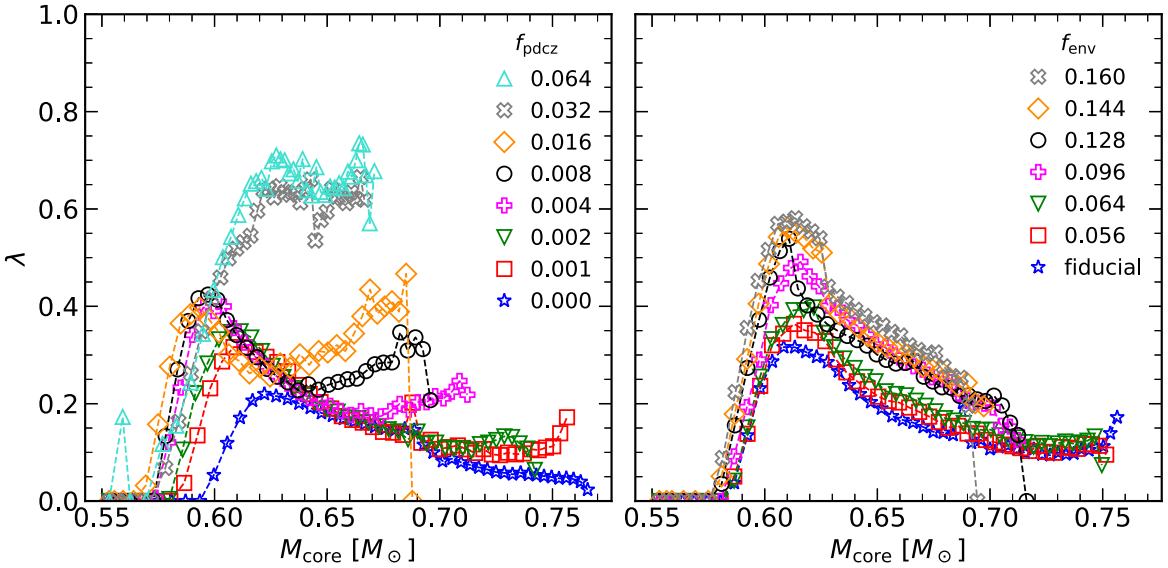

Figure 3. Evolution of λ as a function of the core mass. Both panels show an $M_{ini} = 2.50\ M_\odot$ model. The left panel shows all (0.047^*, f_{pdcz}) models. The right panel shows (f_{env}, 0.001) models. Each symbol corresponds to a thermal pulse.

parameters to prevent potential systematic errors. We also recall that λ is mainly dependent on the core mass and the envelope mass at fixed metallicity (Straniero et al. 2003). These pieces of information serve as our reference point for the subsequent analysis of our TP-AGB tracks.

Figure 3 illustrates the evolution of λ relative to M_{core} for an $M_{ini} = 2.5\ M_\odot$ star for every set. Generally, increasing envelope overshooting leads to a more efficient dredge-up. That is a standard behavior and what is usually found in literature, as increased overshooting depth destabilizes deeper mass shells. In this paper, however, the λ-curves show a unique pattern at varying f_{pdcz}. Again the TDU efficiency increases with the overshooting parameter (in this case, that for the PDCZ), in agreement with Herwig (2000). However, the shape of the λ-curves at varying f_{pdcz} displays a prominent double maximum, instead of the usual bell-like profile (Straniero et al. 1997, 2003; Cristallo et al. 2011; Marigo 2022a). We realize that the second rise of λ with M_{core} begins roughly at M_{tr}, at which the mass-loss rate changes from that of a Blöcker wind to that of the dust-free pulsation-only-driven regime. Thus, we argue that the track is moved back to a region of the (M_{core}, M_{env}) plane where the TDU is favored (Straniero et al. 2003).

It is important to highlight that λ is not sufficient to determine completely the star's evolution. Instead, the interplay of the growth of the core mass with the composition of the dredge-up material should be considered as a pivotal factor. Figure 4 shows an example of the mass-loss rate evolution with time of an $M = 2.50\ M_\odot$ star from the set (0.128, 0.001). Changing f_{env} or f_{pdcz} does affect the evolution, as it changes the transition to a carbon star in the first place, but it also modifies the duration of the dust-free phase with low mass-loss rates. It is not easy to predict how much the total TP-AGB lifetime changes and thus the effect on the core mass, but it is clear that the two overshooting parameters are mildly degenerate. The parameter f_{env} only impacts the TDU efficiency (as shown in Figure 3), while f_{pdcz} changes the intershell composition too, as shown in Figure 5. In general, deeper PDCZ overshooting will increase the carbon abundance in the intershell but it increases oxygen abundance too,

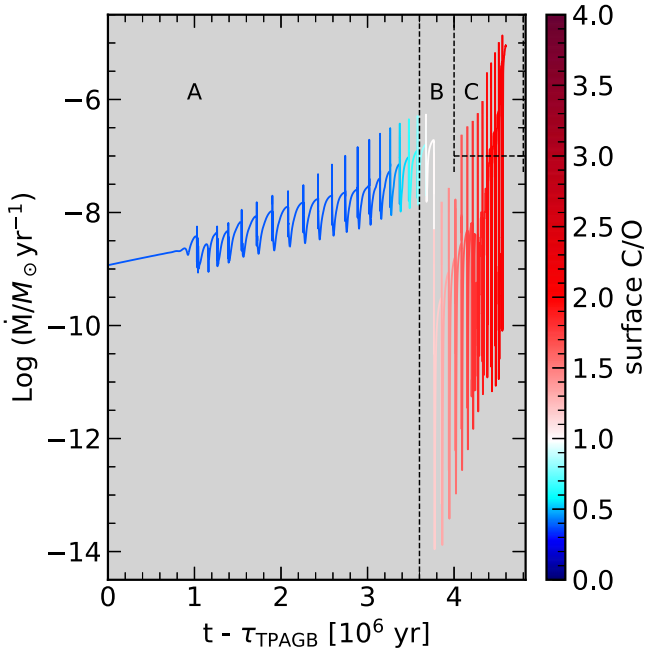

Figure 4. Mass-loss evolution of $M_{ini} = 2.5\ M_\odot$ with $f_{env} = 0.128$ and $f_{pdcz} = 0.001$. The parameter $\tau_{TPAGB} = 1.350$ Gyr is the time spent before the beginning of the TP-AGB. A, B, and C mark the three main regimes of the mass loss. A: wind for O-rich stars (Bloecker 1995); B: dust-free pulsation-driven wind (Marigo et al. 2020); C: carbon-dust-driven wind (Mattsson et al. 2010; Bladh et al. 2019).

decreasing the overall $C/O_{intershell}$ ratio of the material that is being brought to the surface.

After analyzing the effect of f_{env} and f_{pdcz} on λ, we are interested in the impact on the mass threshold previously presented in Figure 2. Clearly, M_{end-he} and M_{1tp} are not affected due to our assumptions. Figure 6 shows how the extension of the overshooting region (in the envelope and PDCZ) affects M_{tdu} and M_{tr}. The effect of f_{env} is limited, as both M_{tdu} and M_{tr} change by less than $0.05\ M_\odot$ in the low-mass range. At $M_{ini} \gtrsim 2.8\ M_\odot$ M_{tdu} does not change (in both cases) because it takes place at the first thermal pulse, which is independent of the overshooting

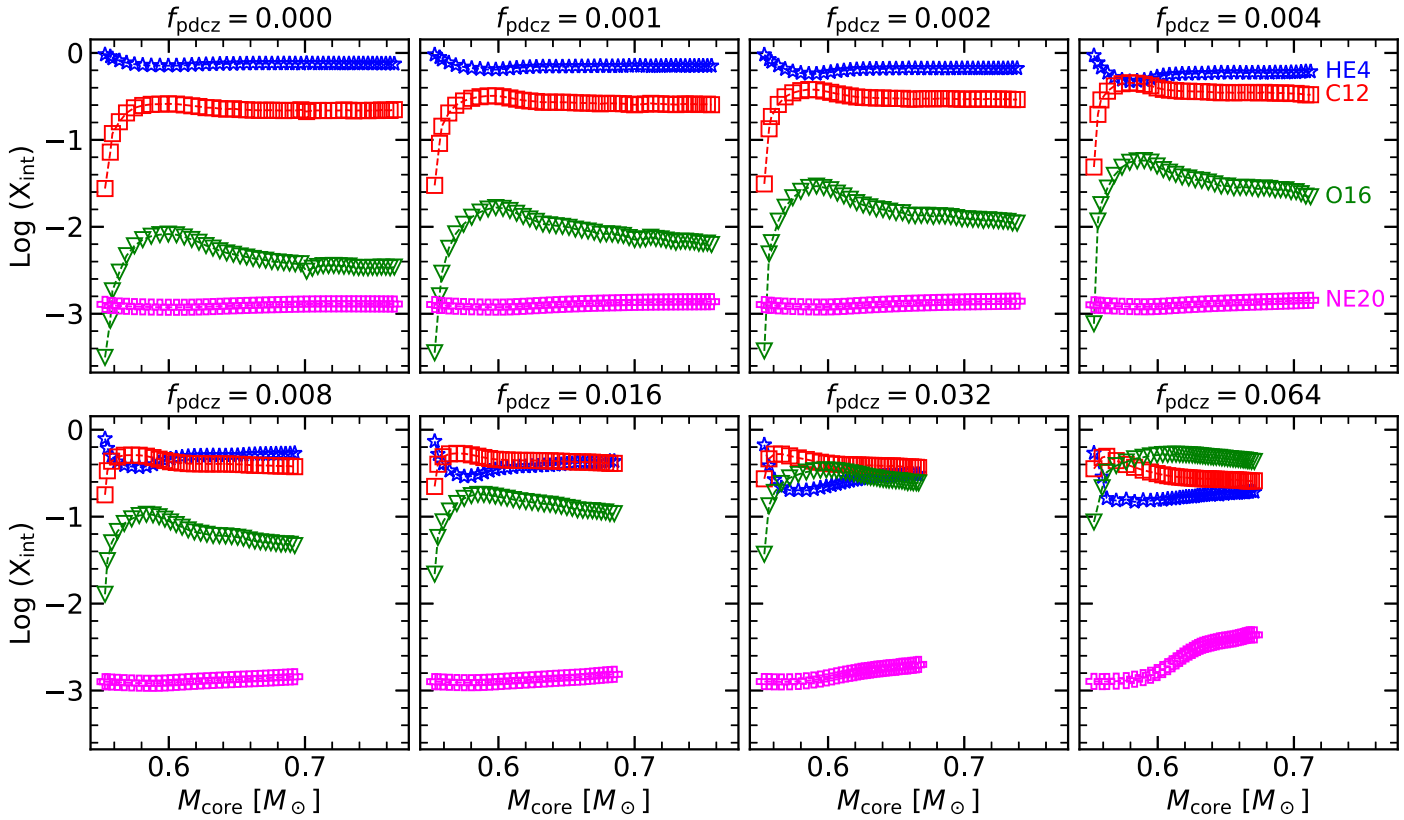

Figure 5. Intershell abundances (in log scale) of ^{4}He, ^{12}C, ^{16}O, and ^{20}Ne after every calculated pulse for every (0.047^*, f_{pdcz}) set and $M_{ini} = 2.50\ M_\odot$.

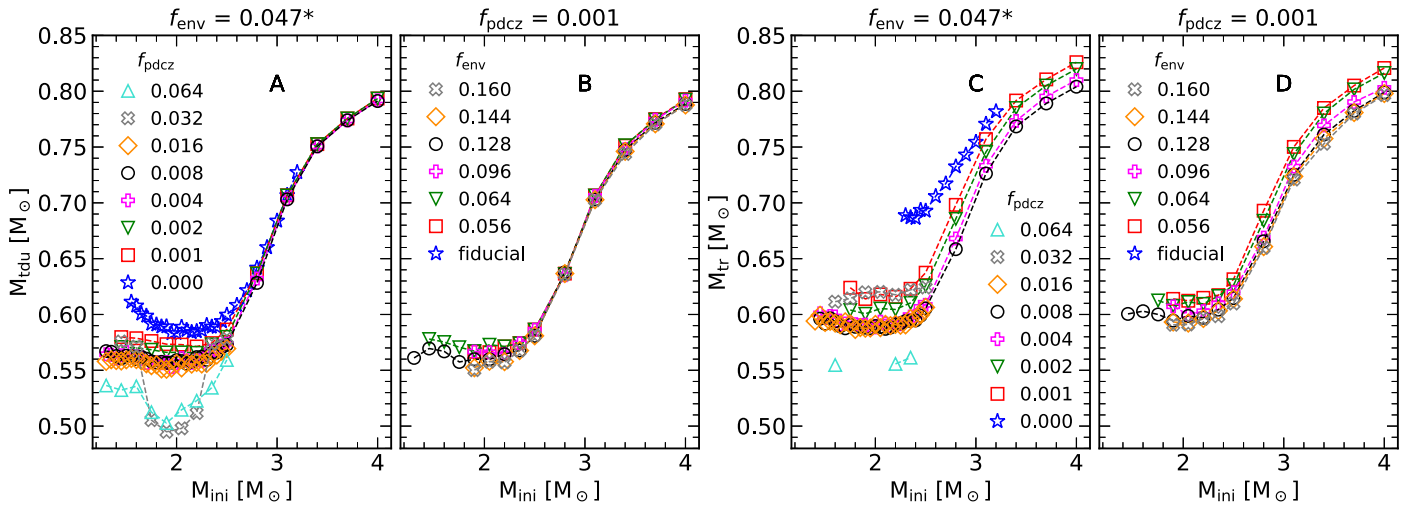

Figure 6. Core mass at the first occurrence of the TDU (A and B panels) and core mass when $C/O_{surf} > 1$ (C and D). The $f_{pdcz} \geqslant 0.016$ models are limited to $M_{ini} \leqslant 2.5\ M_\odot$. The $f_{pdcz} = 0.000$ set is limited to $M_{ini} \leqslant 3.2\ M_\odot$. A and C panels: ($0.047^*$, f_{pdcz}) models. B and D panels: (f_{env}, 0.001) models. The $f_{env} = 0.056$, 0.096, 0.144, 0.160 models are limited to $M_{ini} \geqslant 1.9\ M_\odot$.

parameters. On the other hand f_{pdcz} has a great impact on M_{tdu} and M_{tr}. The first occurrence of the TDU is significantly lowered in core mass at increasing f_{pdcz}, especially for oxygen-rich intershells. Furthermore, the TDU occurs for even lower initial masses, from $M_{ini} \simeq 1.6\ M_\odot$ at $f_{pdcz} = 0.000$ to $M_{ini} \simeq 1.3\ M_\odot$ for $f_{pdcz} \geqslant 0.004$. That is even more evident when looking at the transition core mass M_{tr} from M-type to C-type. A small value for f_{pdcz} is enough to make M_{tr} drop from $\sim 0.7\ M_\odot$ to $\sim 0.63\ M_\odot$. Again, it significantly lowers the threshold for the first (initial) mass becoming C-type from $M_{ini} \simeq 2.3\ M_\odot$ for no PDCZ overshooting to $M_{ini} \simeq 1.4\ M_\odot$ at $f_{pdcz} \simeq 0.008$–0.016. However, for $f_{pdcz} > 0.016$, the trend reverses due to a combination of higher TDU efficiency and a C-deficient intershell, leading to delayed or nonexistent transitions. For the extreme $f_{pdcz} = 0.064$, only three tracks become C-type, but they remain in this phase only for a brief period before reverting to M-type due to dredge-ups from an oxygen-rich intershell.

We have investigated the main effects of the two overshooting parameters and their interplay with mass loss on the quantities that shape the IFMR. These considerations are

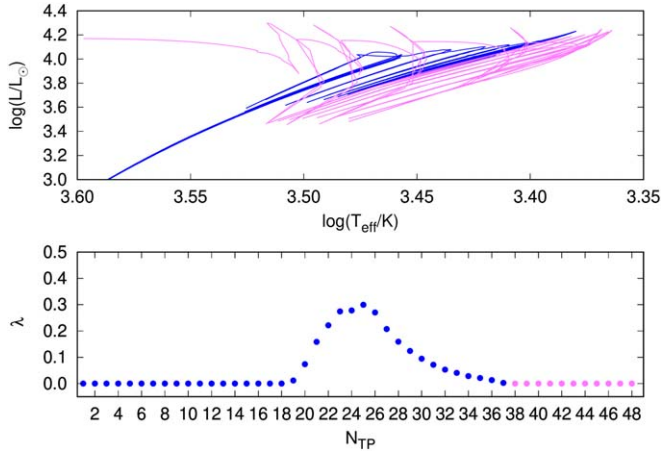

Figure 7. Top panel: evolutionary track of a TP-AGB model with $M_{\rm ini} = 1.85\,M_{\odot}$. PARSEC and COLIBRI sections of the track are colored blue and pink, respectively. Bottom panel: TDU efficiency as a function of the thermal pulse number.

fundamental in shaping the final form of the IFMR, which is discussed in the following section.

4. Estimate of the Final Core Mass

As stars approach the end of the TP-AGB phase, they become characterized by high luminosity ($\log L/L_{\odot} \gtrsim$ 4.2–4.4, depending on the initial mass) and low effective temperature ($\log T_{\rm eff} \lesssim 3.40$). In these advanced phases, issues in finding model convergence arise and it becomes difficult to follow the evolution with PARSEC. This region of the H-R diagram is notorious for numerical difficulties (Wood & Faulkner 1986; Wagenhuber & Weiss 1994; Herwig 2001; Karakas 2003; Miller Bertolami & Althaus 2006; Karakas & Lattanzio 2007; Weiss & Ferguson 2009; Lau et al. 2012). These numerical difficulties appear to be independent of the specific stellar evolution code, computational grid, and time step employed (see also discussion by Addari 2020). We try to determine with our present tracks whether this challenge stems from purely numerical complications or if it originates from more physically motivated grounds; we have not found conclusive information yet, but a full analysis is out of the scope of this work. As a preliminary note, we observe that if the star's envelope is swiftly stripped off (achieved by setting a higher mass-loss rate), the track seamlessly approaches the conclusion of the TP-AGB phase and enters the post-AGB phase. We are aware that the mass loss has a huge impact on TP-AGB evolution, as it sets the lifetime of this phase. Due to our assumptions on stellar winds, particularly the low mass-loss phase (region B in Figure 4), our tracks extend well toward high luminosity and low effective temperature. For this reason, our models usually do not reach the end of the TP-AGB, and the calculation stops a few pulses before the envelope ejection is almost complete.

However, it is still possible to get reliable and self-consistent estimates of the final core mass. First, we employ a simple extrapolation scheme (Section 4.1) to filter out the extreme cases that cannot reproduce the expected IFMR given by Marigo et al. (2020). Then, we complete the remaining models with the COLIBRI code (Marigo et al. 2013), the characteristics of which are briefly summarized in Section 4.2.

4.1. A Simple Estimate

Before applying the COLIBRI code to complete the tracks, we can get a general understanding of the impact of the overshooting parameters by extrapolating over the last thermal pulses. This technique exploits typical key parameters that influence the TP-AGB evolution. These quantities include the core mass $M_{\rm core}$, envelope mass $M_{\rm env}$, mass-loss rate $\dot{M}$, TDU efficiency λ, effective temperature $T_{\rm eff}$, and interpulse period $\tau_{\rm int}$. The procedure is very similar to that adopted by the COLIBRI code but gives up much of its complexity in order to get a simple, yet effective, estimate. Indeed, the process of extrapolating or extending evolutionary models carries the inherent risk of introducing errors or inaccuracies, especially when venturing beyond simulated data points. To account for that, we introduce error bars to the results given by this extrapolation technique, by assuming parameters that intuitively give the smallest and largest core mass growth in the remaining part after PARSEC evolution. We extensively discuss the results of the extrapolation in Section 4.3.

Despite the risk of extending evolutionary models, it is recognized retrospectively that the approach undertaken serves the intended purpose effectively. Specifically, in the context of studying the IFMR, it allows us to gain an initial understanding of the impact of ($f_{\rm env}$, $f_{\rm pdcz}$) on the final core mass. This preliminary set of information is then used to reject some of the possibilities, reducing the set of tracks that then are properly completed with COLIBRI.

4.2. The COLIBRI Code

In comparison to fully synthetic TP-AGB codes (Groenewegen & de Jong 1993; Izzard et al. 2004), the COLIBRI code leaves much of the analytic formalism in favor of detailed physics applied to a complete envelope model, in which the four stellar structure equations are integrated from the atmosphere to the bottom of the hydrogen-burning shell. It incorporates the ÆSOPUS code (Marigo & Aringer 2009; Marigo et al. 2022b) as a routine to calculate the equations of state and Rosseland mean opacities in the star's external layers. Furthermore, it accounts for hot-bottom burning nucleosynthesis and energetics using a nuclear network coupled with a diffusive treatment of convection. The TDU is parameterized, but we recently introduced a more physically sound description in which the TDU efficiency is determined by the core and envelope mass (Marigo 2022a).

Several routines are shared by PARSEC and COLIBRI, including those related to convection, atmosphere, opacities, nuclear reactions, mass loss, and the diffusive treatment of convection in the envelope.

As a result, the COLIBRI code is an appropriate tool for completing the TP-AGB evolution computed by PARSEC. COLIBRI calculations start from the last thermal pulse computed by PARSEC, at the quiescent stage of the pre-flash luminosity maximum. Many structural parameters are loaded into COLIBRI from PARSEC's last model, including the intershell chemical composition, which will be kept constant until the end of the evolution.

Figure 7 shows an example of the matching between PARSEC and COLIBRI computations. This TP-AGB model becomes a carbon star, has a final core mass of $0.726\,M_{\odot}$, and populates the IMFR kink, in agreement with the data (Cummings et al. 2018; Marigo et al. 2020). We also notice

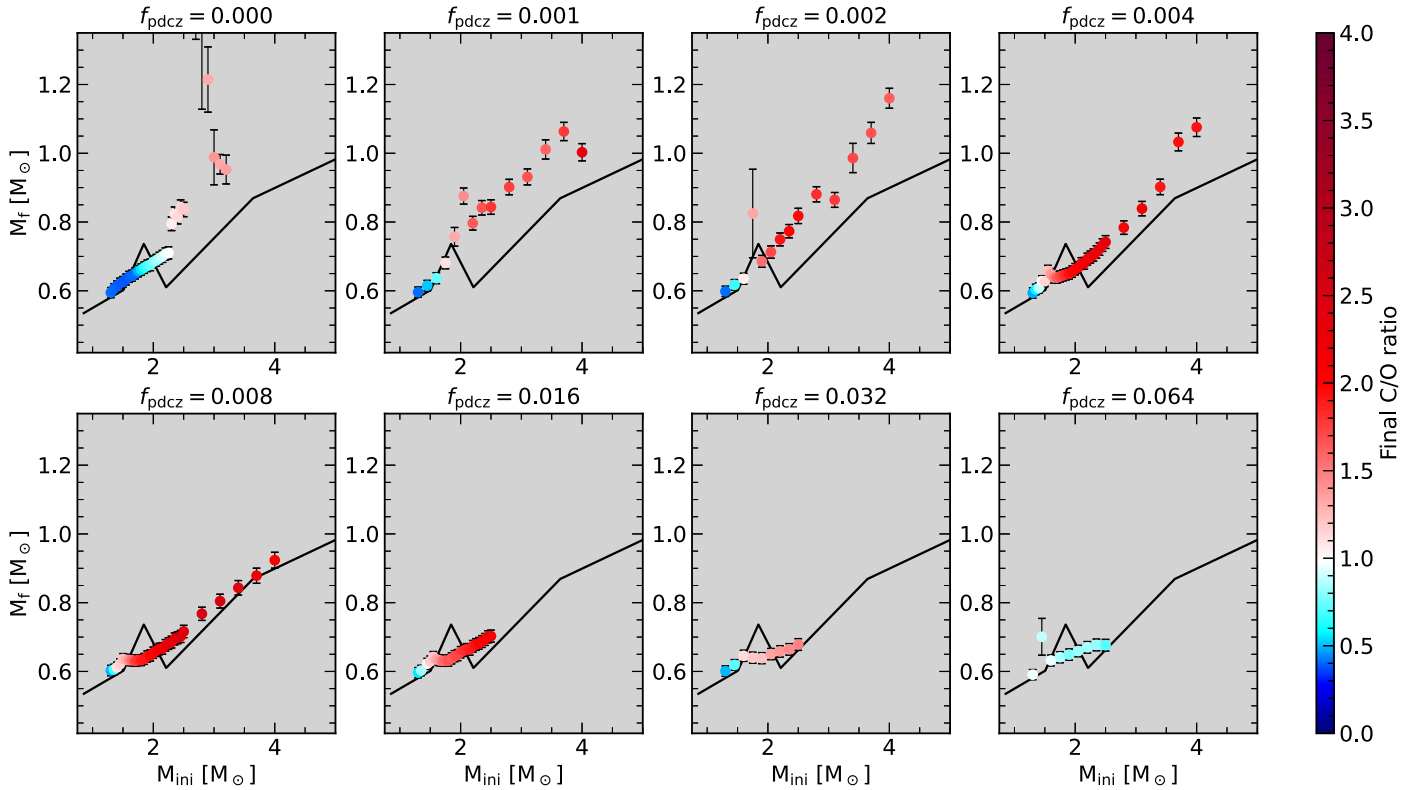

Figure 8. Final core masses for fixed envelope overshooting $f_{env} = 0.047^*$ and varying PDCZ overshooting. The solid line is the semiempirical IFMR found by Marigo et al. (2020). Sets with high overshooting efficiency are limited to $1.3 \leqslant M_{ini}/M_\odot \leqslant 3.2$, which is sufficient to show they are not able to reproduce the IFMR's kink. The final mass is estimated with the extrapolation technique (Section 4.1). A slight oscillation of the result is produced by this technique (see Section 4.1 as well as the error bars).

that the TDU is already quenched when COLIBRI starts the computations. As a consequence, the number of pulses computed with COLIBRI ($N_{COLIBRI}$) is modest in most tracks with $N_{COLIBRI} \simeq 1$–2, except for a few cases, where $N_{COLIBRI} \simeq 8$–10. We will discuss the final results with the complete tracks in the following section.

4.3. Shape of the IFMR

Marigo et al. (2020) demonstrated that the IFMR is not monotonic and exhibits a notable kink between initial masses of around 1.65 and 2.1 $M_\odot$. This kink is attributed to the chemical enrichment brought about by the TDU phenomenon, coupled with the diverse regimes of mass loss as ruled by the carbon excess C − O:

$$\mathrm{C} - \mathrm{O} = \log\left(\frac{n_\mathrm{C} - n_\mathrm{O}}{n_\mathrm{H}}\right) + 12 \quad \text{if} \quad n_\mathrm{C} - n_\mathrm{O} > 0 \qquad (4)$$

where n_i is the number abundance of the i element. Stars with carbon excess less than $8.2 \lesssim (\mathrm{C} - \mathrm{O})_{min} \lesssim 9.2$ experience extended lifetimes, due to weaker winds (B regime in Figure 4), and the core grows above the usual monotonic trend.

One advantage of employing purely synthetic or hybrid evolutionary codes is that the TDU efficiency λ can be treated as a free parameter. The IFMR offers an excellent means to directly calibrate this efficiency without the constraints imposed by more first-principles parameters like convective overshooting efficiency. In this approach, we aim to reproduce the shape of the IFMR by setting the values of (f_{env}, f_{pdcz}), which has a wider impact than simply changing λ.

Figures 8 and 9 illustrate the IFMR for varying f_{pdcz} and f_{env}, respectively. In most cases, a monotonic trend is evident, without any kink. We can notice how the low-mass tracks ($M_{ini} \lesssim 1.5\,M_\odot$) are close to the expected IFMR independently of the choice of parameters. That is because these tracks experience very shallow or no dredge-up, so the core mass has similar evolution even with different (f_{pdcz}, f_{env}). On the other hand, in the intermediate-mass range most of our models overestimate the final mass given by the semiempirical IFMR. The discrepancy is progressively reduced by increasing f_{env} or f_{pdcz}, meaning that a more efficient TDU is needed at these initial masses. This is consistent with previous IFMR calibrations (Marigo et al. 2020; Marigo 2022a), which indicate that λ_{max} increases with the initial mass. Our findings show that a fixed set of overshooting parameters for all masses cannot reproduce the kink at $M_{ini} \simeq 1.65$–$2.10\,M_\odot$.

At this point we still have two parameters that affect the shape of the IFMR. For the rest of the discussion, we fix the value of f_{pdcz} and we increase the efficiency of the TDU by changing f_{env} only, thus fixing the intershell composition (see Figure 5). We will discuss the robustness of this assumption later in this section. In this framework, we can immediately reject the extreme cases $f_{pdcz} = 0.000$ and 0.064. The latter simply does not produce any carbon star. The case with no overshooting in the PDCZ experiences very weak dredge-ups across the whole mass range. Then, the first carbon stars are produced at $M_{ini} \simeq 2.30$–$2.40\,M_\odot$ while we expect to find them at lower masses (Marigo et al. 2022a). Figure 8 shows very clearly that even small values of the PDCZ overshooting, compared to $f_{pdcz} = 0.000$, make the biggest impact on the IFMR. Sets with $f_{pdcz} = 0.001$–0.002 are already enough to

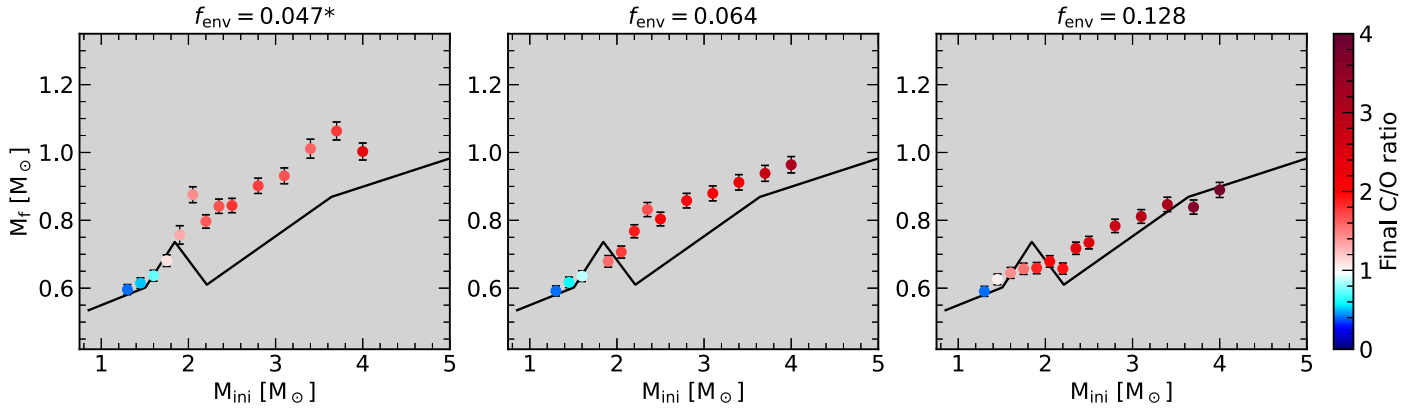

Figure 9. Final core masses for fixed PDCZ overshooting $f_{pdcz} = 0.001$ and varying envelope overshooting. The solid line is a fit to the semiempirical IFMR of Marigo et al. (2020) and Cummings et al. (2018). The final mass is estimated with the extrapolation technique (Section 4.1).

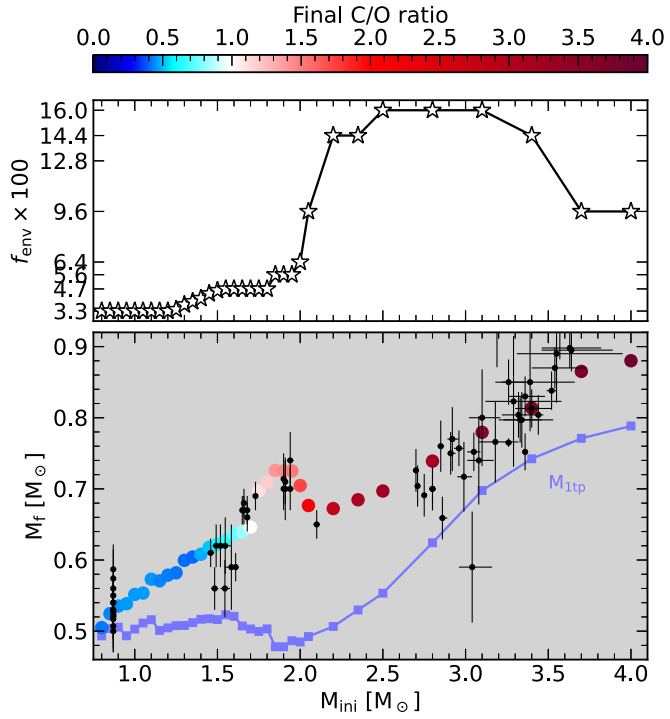

Figure 10. Bottom panel: comparison between the semiempirical IFMR (points with error bars; Cummings et al. 2018; Marigo et al. 2020) and the theoretical predictions of this work (filled circles) color-coded as a function of the final surface C/O. The final mass is reached with COLIBRI as explained in Section 4.2. The core mass at the first thermal pulse M_{1tp} is plotted for reference. Top panel: the corresponding value of envelope overshooting, multiplied by 100 for visualization purposes.

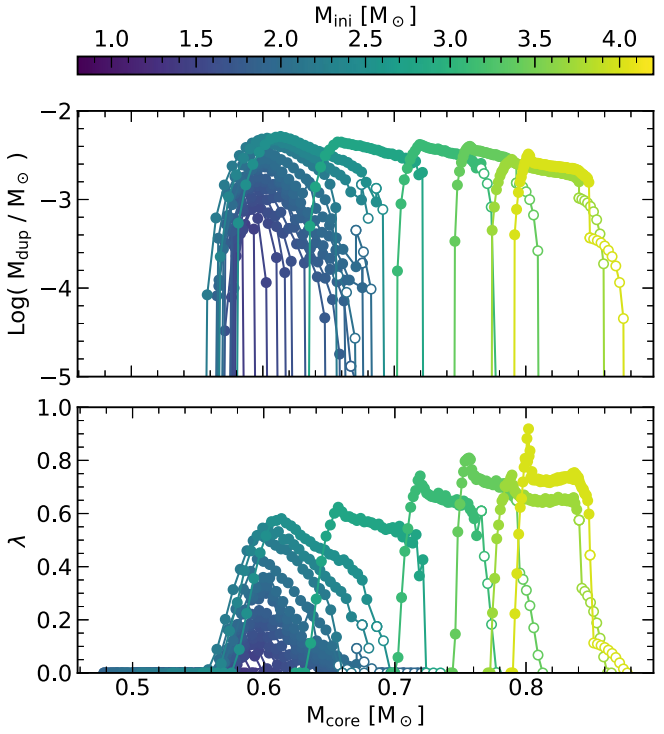

Figure 11. Bottom panel: TDU efficiency vs. current core mass for the tracks used in Figure 10. PARSEC TDUs are marked by filled circles, and COLIBRI TDUs are marked with empty circles. Top panel: log10 of the dredge-up mass vs. the current core mass for the same tracks and symbols.

accommodate all initial masses up to the kink maximum at $M_{ini} \simeq 1.85\,M_\odot$. To select our optimal final set we select $f_{pdcz} = 0.001$, as $f_{pdcz} > 0.002$ produce too efficient TDU events (in terms of both envelope penetration and carbon abundance in the intershell) with the fiducial value ($f_{env} = 0.047^*$) of envelope overshooting. Having set f_{pdcz}, we can just vary f_{env} until a satisfactory fit is achieved, and we can complete these tracks with COLIBRI to find more accurate estimates of the final mass. Figure 10 shows the final IFMR on top of observational data used in previous works (Cummings et al. 2018; Marigo et al. 2020; Canton et al. 2021) and Figure 11 shows the impact of each dredge-up on the same set of tracks. We collect the properties of the final set of tracks in Table 3.

As expected, the negative slope region ($M_{ini} \simeq 1.85$–$2.20\,M_\odot$) indicates an increasing f_{env}, even up to four times greater than the envelope undershooting extension in the lower-mass range. Another change of slope is evident at $M_{ini} \sim 3.50\,M_\odot$, where a reduction in f_{env} is necessary to accommodate larger core growth. In this high-mass range, core growth is severely hampered during the interpulse phase by the combination of a high-efficiency TDU and hot-bottom burning. However, the white dwarf data spread for $M_{ini} \simeq 3.00\,M_\odot$ gives looser constraints on the f_{env} and we select an average value of f_{env}. Figure 11 shows again that PARSEC calculation stops close to the end of the TP-AGB, where the TDU is quenched. Then, it is clear that COLIBRI has a limited impact on the results. Nevertheless, it stands out as a very efficient and powerful tool to complete the TP-AGB evolution, where full stellar evolutionary codes usually give up.

Table 3
Relevant Data for the Final Track Set

M_{ini}	f_{env}	N_{TP}	$N_{COLIBRI}$	$M_{f,\ PARSEC}$	$M_{f,COLIBRI}$	$(C/O)_f$	τ_{HB}	τ_{EAGB}	τ_{TPAGB}	R_2	τ_C	λ_{max}
0.80	0.033	6	...	0.503	...	0.424	102.510	16.129	1.455	0.172	0.000	0.000
0.85	0.033	6	...	0.523	...	0.441	111.940	11.547	1.791	0.119	0.000	0.000
0.90	0.033	7	...	0.534	...	0.455	109.881	11.492	1.963	0.122	0.000	0.000
0.95	0.033	11	...	0.538	...	0.464	113.405	14.591	2.498	0.151	0.000	0.000
1.00	0.033	10	...	0.551	...	0.462	108.428	12.715	2.545	0.141	0.000	0.000
1.05	0.033	9	...	0.554	...	0.468	118.934	9.192	2.070	0.095	0.000	0.000
1.10	0.033	10	...	0.573	...	0.458	112.987	9.563	2.394	0.106	0.000	0.000
1.15	0.033	14	...	0.571	...	0.438	109.913	14.758	2.908	0.161	0.000	0.000
1.20	0.033	14	...	0.579	...	0.428	111.067	13.911	2.952	0.152	0.000	0.000
1.25	0.034	14	...	0.582	...	0.418	108.358	13.055	2.841	0.147	0.000	0.000
1.30	0.037	17	1	0.598	0.599	0.413	107.687	12.026	3.018	0.140	0.000	0.000
1.35	0.039	16	1	0.600	0.604	0.406	113.896	10.045	2.935	0.114	0.000	0.000
1.40	0.041	15	2	0.598	0.608	0.487	120.513	8.452	2.786	0.093	0.000	0.063
1.45	0.044	17	1	0.614	0.618	0.520	103.378	11.132	2.914	0.136	0.000	0.072
1.50	0.046	18	1	0.616	0.622	0.581	108.628	10.258	2.972	0.122	0.000	0.106
1.55	0.047	17	2	0.617	0.627	0.641	121.401	7.263	2.782	0.083	0.000	0.110
1.60	0.047	20	1	0.635	0.637	0.741	113.248	9.355	3.055	0.110	0.000	0.137
1.65	0.047	23	1	0.634	0.640	0.830	129.538	10.010	3.510	0.104	0.000	0.169
1.70	0.047	25	2	0.638	0.646	0.982	117.913	13.553	3.812	0.147	0.000	0.190
1.75	0.047	34	4	0.679	0.697	1.103	129.467	14.204	4.311	0.143	0.657	0.210
1.80	0.047	34	5	0.684	0.709	1.182	159.252	8.776	4.283	0.082	0.789	0.235
1.85	0.056	38	10	0.672	0.726	1.401	267.388	17.313	5.252	0.084	1.014	0.299
1.90	0.056	38	12	0.662	0.725	1.454	234.687	17.506	5.149	0.097	0.890	0.321
1.95	0.056	38	8	0.676	0.725	1.518	240.711	14.036	5.029	0.079	0.975	0.329
2.00	0.064	37	6	0.671	0.705	1.727	195.418	18.703	4.962	0.121	0.925	0.360
2.05	0.096	34	4	0.657	0.677	2.127	193.298	15.462	4.690	0.104	0.939	0.429
2.20	0.144	34	2	0.660	0.672	2.788	154.412	11.410	4.218	0.101	1.073	0.519
2.35	0.144	34	1	0.675	0.685	3.130	126.222	8.305	3.476	0.093	1.115	0.547
2.50	0.160	34	2	0.686	0.697	3.287	95.420	8.453	2.935	0.119	1.193	0.581
2.80	0.160	35	3	0.724	0.739	3.219	63.693	5.019	1.818	0.107	0.905	0.624
3.10	0.160	38	4	0.766	0.779	3.571	43.372	3.239	1.194	0.102	0.663	0.742
3.40	0.144	41	7	0.793	0.814	3.626	29.673	2.559	0.955	0.118	0.583	0.809
3.70	0.096	62	10	0.841	0.865	3.681	23.604	1.559	0.885	0.104	0.563	0.745
4.00	0.096	71	11	0.849	0.880	3.901	17.128	1.360	0.859	0.130	0.584	0.919

Notes. All tracks have $f_{pdcz} = 0.001$. N_{TP} is the number of pulses calculated by PARSEC. $N_{COLIBRI}$ is the number of thermal pulses calculated by COLIBRI. $M_{f,\ PARSEC}$ is the core mass reached by PARSEC, and $M_{f,\ COLIBRI}$ is the final core mass calculated by continuing the evolution with COLIBRI. The parameter τ_{HB} is the time spent in the core He-burning phase; τ_{EAGB} is the time spent in the early AGB, from the central He exhaustion to the beginning of the TP-AGB, set when the helium intershell thickness becomes smaller than 0.1 $M_\odot$; τ_{TPAGB} is the time spent in the TP-AGB phase; and τ_C is the time spent as a C-type star. The R_2 ratio is estimated as $(\tau_{EAGB} + \tau_{TPAGB})/\tau_{HB}$. Masses are in solar units and ages in Myr.

Finally, we want to briefly discuss the robustness of the results when giving up the assumption of fixed f_{pdcz}. If we let both parameters be free, a simple χ^2 fit gives a random distribution of (f_{env}, f_{pdcz}), with no clear trend with the initial mass. Still leaving it as an open possibility, it would give little or no information on the internal mixing processes and on the efficiency of the TDU. That is because the parameters change not only the envelope penetration but also the intershell composition, thus leading to a mild degeneracy of the parameters. The works by Wagstaff et al. (2020) and Addari (2020) give useful hints on how to overcome this apparent degeneracy. The [WC] type of central stars of planetary nebula abundances reflects the intershell composition, giving tighter constraints on the f_{pdcz} only. These findings compel us to select a value for f_{pdcz}, and let only f_{env} vary to adjust the efficiency of the TDU. Herwig (2005) and Wagstaff et al. (2020) suggest $0.004 < f_{pdcz} < 0.016$, which is much higher than the $f_{pdcz} = 0.001$ found in this work based on the IFMR. However, the typical errors for PG 1159 stars' abundances (about 0.3–0.5 dex; Werner & Herwig 2006; Werner & Rauch 2014; Werner et al. 2016) and the data spread make it difficult to differentiate between scenarios with low or zero f_{pdcz}, by relying solely on intershell abundances. Given the intricacies in interpreting observations, primarily due to the potential influence of late thermal pulses, the study of [WC]-type central stars of planetary nebulae is beyond the scope of this work, but we acknowledge that coupling this data with the IFMR can potentially lift the degeneracy of (f_{env}, f_{pdcz}).

5. Concluding Remarks

This study undertook a comprehensive exploration of a broad spectrum of values for both envelope and PDCZ overshooting, aiming to calibrate them in accordance with the semiempirical IFMR presented by Marigo et al. (2020). Notably, this work stands as the first successful endeavor in reproducing the IFMR kink employing a full stellar evolution code, PARSEC, supported by the COLIBRI code. Given that PARSEC stops in close proximity to the end of the evolution, where the TDU is no longer relevant in shaping the core mass, and considering the inherent scatter in observational data, the validity of our scheme is evident.

It is worth noting that the previous TDU calibration based on the semiempirical IFMR performed by Marigo et al. (2020) and Marigo (2022a) is supported by this work. White dwarfs populating the kink had progenitor carbon stars that experienced shallow mixing events ($\lambda_{\rm max} \lesssim 0.2$) with mild carbon enrichment and modest mass-loss rates. Then, the efficiency of the TDU increases with increasing initial mass in both the PARSEC and COLIBRI codes. This suggests that the efficient computational capabilities of the COLIBRI code make it a valuable tool for both exploring the parameter space and potentially indicating a calibration pathway.

In this study, we show that the fiducial value of envelope overshooting ($f_{\rm env} = 0.047^{*}$) alone falls short of explaining the observed outcomes, as such tracks dredge up minimal amounts of mass. Our investigation establishes that a constant envelope penetration is not a viable solution either. On the other hand, a small value for the PDCZ overshooting ($f_{\rm pdcz} = 0.001$) with a varying $f_{\rm env}$ (Figure 10, top panel) proves sufficient to approach a feasible solution in reproducing the IFMR. This work may serve as a practical guideline, focusing on the extent of the envelope penetration (Figure 11) and the composition of the intershell (Figure 5, panel $f_{\rm pdcz} = 0.001$). The cumulative effects of these two factors directly influence mass loss, ultimately shaping the star's evolution to align with the observed IFMR. However, we noted a mild degree of degeneracy between the two overshooting parameters. Our future exploration will go deeper into this aspect, by combining the present results with information from observed intershell composition from [WC]-type central stars of planetary nebulae (Wagstaff et al. 2020). This extension holds the potential to constrain the value of $f_{\rm pdcz}$ independently, thus leaving only the envelope overshooting efficiency as a free parameter.

Acknowledgments

P.M., F.A., A.B., and G.V. acknowledge funding support by the Italian Ministerial Grant PRIN 2022, "Radiative opacities for astrophysical applications," No. 2022NEXMP8, CUP C53D23001220006. G.C. acknowledges support from the Agence Nationale de la Recherche grant POPSYCLE No. ANR-19-CE31-0022. We thank the anonymous referee for providing valuable comments that helped to improve this manuscript.

Appendix
Shell Shifting

The concept of shell shifting was initially introduced by Weigert (1966). This idea stems directly from the principle of energy conservation. The variation in the hydrogen profile during an interpulse phase can be expressed as follows:

$$\frac{\partial X}{\partial M}\left(\frac{L_{\rm shell}}{X_{\rm env} Q}\right) = \frac{\varepsilon}{Q} \tag{A1}$$

where X is the hydrogen abundance ($X_{\rm env}$ the one in the convective envelope), $L_{\rm shell}$ is the hydrogen-burning luminosity generated in the H-shell, Q is the effective q-value of the nuclear network, ϵ is the nuclear energy generation rate, and finally M is the mass coordinate. Equation (A1) was used to determine the hydrogen profile following the expansion of the core by a certain amount. This approach demonstrated good agreement with calculations using small time steps, albeit with the caveat that computational power in the 1960s was significantly more limited than today's standards. Nevertheless, contemporary stellar evolution codes have evolved to become more comprehensive, and TP-AGB models, in particular, remain computationally intensive.

Stancliffe et al. (2005) studied the difference between using simultaneous and nonsimultaneous solvers in stellar evolution codes. In conclusion, they observed that the only difference is that the second type of codes only needs shorter time steps to produce the same results, and there is no inherent problem with using a nonsimultaneous method of solution. However, shorter time steps considerably increase computational time. To address this issue, we have introduced a modified shell-shifting procedure to use during interpulse periods. Diverging from the original method employed by Weigert (1966), our approach involves applying the same principle to refine the solution provided by the chemical module solver. Instead of keeping the structure fixed while solving the nuclear network, we adjust the temperature and density profiles based on the observed shifts in the hydrogen profile. This innovation permits the use of considerably longer time steps, extending from the range of 1–10 yr to 100–1000 yr. Additionally, we introduce an energy conservation validation mechanism, which is based on an enhanced version of Equation (A1). This validation procedure considers both the hydrogen abundance at the shell's upper boundary and the collective effective q-value of all hydrogen-burning reactions. This validation step refines the final time step allocated for the chemical solution by introducing a corrective factor that ensures Equation (A1) is respected.

This refined approach substantially reduces computational time, approximately by a third as compared to the case of utilizing small time steps, while incurring minimal to no loss in accuracy concerning core growth and energy conservation.

We compute a test track with and without the shell-shifting approach, not changing any other physical or numerical input, and we summarize the result in Figure 12. All physical quantities are in good agreement between the two cases, with only minimal differences in the first few pulses. With a minimal accuracy cost, the method can speed up computing time and save storage. In the last panel of Figure 12, the number of models per pulse cycle is shown against the core mass. The shell-shifting track keeps a constant number of models (about 4000 timestamps) against a steeply rising trend topping at about 16,000 models, gaining a factor of ∼3–4 of CPU time.

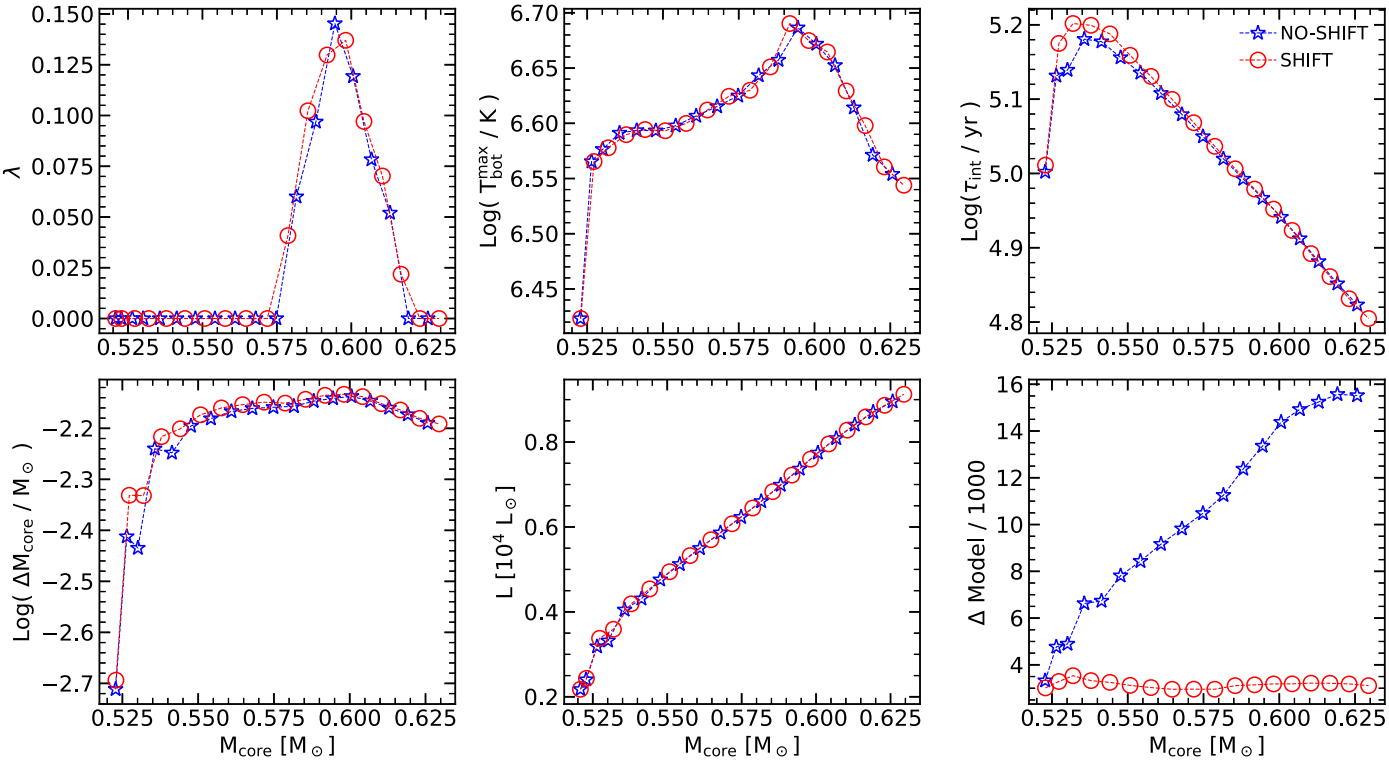

Figure 12. Comparison of the same track $M_{\rm ini} = 1.60\ M_\odot$ from the (0.047, 0.001) set computed with shell shifting (SHIFT) and no shell shifting (NO-SHIFT). Top row, from left to right: TDU efficiency, temperature maximum at the bottom of the convective envelope, and interpulse time against core mass. Bottom row, from left to right: core growth per pulse cycle, maximum quiescent luminosity, and number of models per pulse cycle against core mass.

ORCID iDs

Francesco Addari https://orcid.org/0000-0002-3867-9966
Paola Marigo https://orcid.org/0000-0002-9137-0773
Alessandro Bressan https://orcid.org/0000-0002-7922-8440
Guglielmo Costa https://orcid.org/0000-0002-6213-6988
Kendall Shepherd https://orcid.org/0000-0001-5231-0631
Guglielmo Volpato https://orcid.org/0000-0002-8691-4940

References

Addari, F. 2020, MA thesis, Univ. of Padua, https://thesis.unipd.it/handle/20.500.12608/22550
Alongi, M., Bertelli, G., Bressan, A., & Chiosi, C. 1991, A&A, 244, 95
Bladh, S., Eriksson, K., Marigo, P., Liljegren, S., & Aringer, B. 2019, A&A, 623, A119
Bloecker, T. 1995, A&A, 297, 727
Böhm-Vitense, E. 1958, ZAp, 46, 108
Bressan, A., Bertelli, G., & Chiosi, C. 1986, MmSAI, 57, 411
Bressan, A., Girardi, L., Marigo, P., Rosenfield, P., & Tang, J. 2015, Asteroseismology of Stellar Populations in the Milky Way, Vol. 39 (Berlin: Springer), 25
Bressan, A., Marigo, P., Girardi, L., et al. 2012, MNRAS, 427, 127
Bressan, A. G., Chiosi, C., & Bertelli, G. 1981, A&A, 102, 25
Caffau, E., Ludwig, H.-G., Steffen, M., Freytag, B., & Bonifacio, P. 2011, SoPh, 268, 255
Canton, P. A., Williams, K. A., Kilic, M., & Bolte, M. 2021, AJ, 161, 169
Castellani, V., Chieffi, A., Tornambe, A., & Pulone, L. 1985, ApJ, 296, 204
Chen, Y., Girardi, L., Bressan, A., et al. 2014, MNRAS, 444, 2525
Choi, J., Dotter, A., Conroy, C., et al. 2016, ApJ, 823, 102
Christensen-Dalsgaard, J., Monteiro, M. J. P. F. G., Rempel, M., & Thompson, M. J. 2011, MNRAS, 414, 1158
Constantino, T., Campbell, S. W., Lattanzio, J. C., & van Duijneveldt, A. 2016, MNRAS, 456, 3866
Costa, G., Bressan, A., Mapelli, M., et al. 2021, MNRAS, 501, 4514
Costa, G., Girardi, L., Bressan, A., et al. 2019a, A&A, 631, A128
Costa, G., Girardi, L., Bressan, A., et al. 2019b, MNRAS, 485, 4641
Cranmer, S. R., & Saar, S. H. 2011, ApJ, 741, 54
Cristallo, S., Piersanti, L., Straniero, O., et al. 2011, ApJS, 197, 17
Cummings, J. D., Kalirai, J. S., Choi, J., et al. 2019, ApJL, 871, L18
Cummings, J. D., Kalirai, J. S., Tremblay, P.-E., Ramirez-Ruiz, E., & Choi, J. 2018, ApJ, 866, 21
Dotter, A. 2016, ApJS, 222, 8
Eriksson, K., Nowotny, W., Höfner, S., Aringer, B., & Wachter, A. 2014, A&A, 566, A95
Frost, C. A., & Lattanzio, J. C. 1996, ApJ, 473, 383
Fu, X., Bressan, A., Marigo, P., et al. 2018, MNRAS, 476, 496
Groenewegen, M. A. T., & de Jong, T. 1993, A&A, 267, 410
Herwig, F. 2000, A&A, 360, 952
Herwig, F. 2001, Ap&SS, 275, 15
Herwig, F. 2005, ARA&A, 43, 435
Iglesias, C. A., & Rogers, F. J. 1996, ApJ, 464, 943
Itoh, N., Uchida, S., Sakamoto, Y., Kohyama, Y., & Nozawa, S. 2008, ApJ, 677, 495
Izzard, R. G., Tout, C. A., Karakas, A. I., & Pols, O. R. 2004, MNRAS, 350, 407
Kalirai, J. S., Davis, D. S., Richer, H. B., et al. 2009, ApJ, 705, 408
Kalirai, J. S., Hansen, B. M. S., Kelson, D. D., et al. 2008, ApJ, 676, 594
Kalirai, J. S., Marigo, P., & Tremblay, P.-E. 2014, ApJ, 782, 17
Karakas, A., & Lattanzio, J. C. 2007, PASA, 24, 103
Karakas, A. I. 2003, PhD thesis, Monash Univ.
Karakas, A. I. 2014, MNRAS, 445, 347
Karakas, A. I., & Lattanzio, J. C. 2014, PASA, 31, e030
Komatsu, E., Smith, K. M., Dunkley, J., et al. 2011, ApJS, 192, 18
Lattanzio, J. C., Tout, C. A., Neumerzhitckii, E. V., Karakas, A. I., & Lesa, P. 2017, MmSAI, 88, 248
Lau, H. H. B., Gil-Pons, P., Doherty, C., & Lattanzio, J. 2012, A&A, 542, A1
Marigo, P. 2013, in IAU Symp. 281, Binary Paths to Type Ia Supernovae Explosions, ed. R. Di Stefano, M. Orio, & M. Moe (Cambridge: Cambridge Univ. Press), 36
Marigo, P. 2022a, Univ, 8, 243
Marigo, P. 2022b, in IAU Symp. 366, The Origin of Outflows in Evolved Stars (Cambridge: Cambridge Univ. Press), 216
Marigo, P., & Aringer, B. 2009, A&A, 508, 1539
Marigo, P., Aringer, B., Girardi, L., & Bressan, A. 2022b, ApJ, 940, 129
Marigo, P., Bossini, D., Trabucchi, M., et al. 2022a, ApJS, 258, 43
Marigo, P., Bressan, A., Nanni, A., Girardi, L., & Pumo, M. L. 2013, MNRAS, 434, 488

Marigo, P., Cummings, J. D., Curtis, J. L., et al. 2020, NatAs, 4, 1102
Marigo, P., & Girardi, L. 2007, A&A, 469, 239
Marigo, P., Girardi, L., & Bressan, A. 1999, A&A, 344, 123
Mattsson, L., Wahlin, R., & Höfner, S. 2010, A&A, 509, A14
Miller Bertolami, M. M., & Althaus, L. G. 2006, A&A, 454, 845
Mowlavi, N. 1999, A&A, 344, 617
Nguyen, C. T., Costa, G., Girardi, L., et al. 2022, A&A, 665, A126
Pastorelli, G., Marigo, P., Girardi, L., et al. 2019, MNRAS, 485, 5666
Pastorelli, G., Marigo, P., Girardi, L., et al. 2020, MNRAS, 498, 3283
Reimers, D. 1975, MSRSL, 8, 369
Salaris, M., Serenelli, A., Weiss, A., & Miller Bertolami, M. 2009, ApJ, 692, 1013
Saumon, D., Blouin, S., & Tremblay, P.-E. 2022, PhR, 988, 1
Stancliffe, R. J., Izzard, R. G., & Tout, C. A. 2005, MNRAS, 356, L1
Straniero, O., Chieffi, A., Limongi, M., et al. 1997, ApJ, 478, 332
Straniero, O., Domínguez, I., Cristallo, S., & Gallino, R. 2003, PASA, 20, 389
Sweigart, A. V., & Demarque, P. 1973, in IAU Colloq. 21, Variable Stars in Globular Clusters and in Related Systems (Dordrecht: Reidel), 221
Tang, J., Bressan, A., Rosenfield, P., et al. 2014, MNRAS, 445, 4287
Ventura, P., Karakas, A., Dell'Agli, F., García-Hernández, D. A., & Guzman-Ramirez, L. 2018, MNRAS, 475, 2282
Wagenhuber, J., & Weiss, A. 1994, A&A, 290, 807
Wagstaff, G., Bertolami, M. M. M., & Weiß, A. 2020, MNRAS, 493, 4748
Weidemann, V. 2000, A&A, 363, 647
Weigert, A. 1966, ZA, 64, 395
Weiss, A., & Ferguson, J. W. 2009, A&A, 508, 1343
Werner, K., & Herwig, F. 2006, PASP, 118, 183
Werner, K., & Rauch, T. 2014, A&A, 569, A99
Werner, K., Rauch, T., & Kruk, J. W. 2016, A&A, 593, A104
Williams, K. A., Bolte, M., & Koester, D. 2004, ApJL, 615, L49
Williams, K. A., Bolte, M., & Koester, D. 2009, ApJ, 693, 355
Winters, J. M., Bertre, T. L., Jeong, K. S., Helling, C., & Sedlmayr, E. 2000, A&A, 361, 641
Wood, P. R., & Faulkner, D. J. 1986, ApJ, 307, 659